# Investigation on Jet Characteristics of Turbofan Exhaust System under Take-off Condition with High Angle of Attack

Z. X. Wang, W. J. Wang, L. Zhou†, W. J. Deng and J. W. Shi

*Shaanxi Key Laboratory of Internal Aerodynamics in Aero-Engine, School of Power and Energy, Northwestern Polytechnical University, Xi'an, 710072, People's Republic of China*

†*Corresponding Author Email: zhouli@nwpu.edu.cn*

## ABSTRACT

To understand the jet flow characteristics of turbofan separate exhaust system, a parametric design method based on the initial Class Shape Transformation function was developed. HBPR and UHBPR turbofan separate exhaust systems were designed. Furthermore, the jet flow characteristics of the HBPR turbofan exhaust system under take-off condition with zero angle of attack were studied based on numerical simulation. The jet flow characteristics of the HBPR and UHBPR turbofan exhaust system under take-off condition with high angle of attack were also simulated. The effects of angle of attack and bypass ratio on the jet flow characteristics were investigated and the related flow mechanisms were analyzed. Results show that the axisymmetric plumes of the HBPR turbofan exhaust system are distributed around the engine axis under take-off condition with zero angle of attack. With the plug wake as the center, the core flow, the fan/core shear layer, the fan flow, the fan/free stream shear layer and the free stream are wrapped around the plug wake from inside out. Vortexes appear in the lee area at the back of the cowl and jet flow under take-off condition with high angle of attack. These vortexes cause cross sectional secondary flow and expose the high-velocity core flow to the low-velocity free stream. The contact area and velocity gradient in the mixing region among the free stream, fan flow and core flow increase. Therefore, the mixture among jet flow and free stream strengthens. So the high-velocity region, the high-vorticity region, and the high turbulence kinetic energy region shorten by 55.1%, 47.7% and 50.9% respectively. The vorticity values and turbulence kinetic energy level peak on the upper side of the exhaust plumes increase by about 30% and 87% respectively. Relative to these parameters from the HBPR turbofan exhaust system, the jet velocity peak value of UHBPR turbofan decreases by 5.5% under take-off condition with high angle of attack. The vorticity values and turbulence kinetic energy level reduce due to decreased velocity gradient in shear layers downstream of the nozzle exit plane. The turbulence kinetic energy level peak on the upper side of the exhaust plumes decreases by 29.3%. The reasons are that the contact area between high-velocity core flow and the free stream decreases due to thicker fan flow and the velocity gradient in the core flow and free stream mixing region decreases because of the lower core flow velocity.

Keywords: Jet characteristics; Exhaust system; Take-off condition; High angle of attack; Turbofan.

## NOMENCLATURE

| | | | |
|---|---|---|---|
| $A_9$ | exit area of core nozzle | iCST | initial Class Shape Transformation function |
| $A_{19}$ | exit area of fan nozzle | | |
| $A_E$ | nozzle exit area | $k$ | specific heat ratio |
| $A_i$ | area at the location of $i^{th}$ point | $L_{CN}$ | core nozzle length |
| $CNEA$ | Core Nozzle Exit Angle | $L_{FN}$ | fan nozzle length |
| $CNPR$ | Core Nozzle Pressure Ratio | $L_{NC}$ | Mid-surface profile length of nozzle |
| $D_m$ | maximum diameter of nacelle | $Ma_9$ | Mach number at core nozzle exit |
| $FNEA$ | Fan Nozzle Exit Angle | $Ma_{19}$ | Mach number at fan nozzle exit |
| $FNPR$ | Fan Nozzle Pressure Ratio | $MFCR$ | Mass Flow Capture Ratio |
| $H$ | flight height | $NEA$ | Nozzle Exit Angle |
| $I$ | number of selected points in mid-surface profile | $p_{amb}$ | ambient pressure |
| | | $p_t$ | total pressure |

| | | | |
|---|---|---|---|
| $p_{t13}$ | total pressure at the inlet of fan nozzle | $R$ | gas constant |
| $p_{t5}$ | total pressure at the inlet of core nozzle | $T_{t13}$ | total temperature at the inlet of fan nozzle |
| $R_{19O}$ | outer radius at fan nozzle exit | | |
| $R_{22I}$ | inner radius at the inlet of fan nozzle | $T_{t5}$ | total temperature at the inlet of core nozzle |
| $R_{22O}$ | outer radius at the inlet of fan nozzle | | |
| $R_{5I}$ | inner radius at the inlet of core nozzle | $\sigma_{CN}$ | pressure recovery coefficient of core nozzle |
| $R_{5O}$ | *outer radius at the inlet of core nozzle* | | |
| $R_{9O}$ | *outer radius at core nozzle exit* | $\sigma_{FN}$ | pressure recovery coefficient of fan nozzle |
| $R_{EC}$ | *radius at mid-surface profile exit* | | |
| $R_{NC, i}$ | radial coordinate of $i^{th}$ point in mid-surface profile | $W_5$ | core nozzle mass flow rate |
| | | $W_{13}$ | fan nozzle mass flow rate |
| $R_{NI, i}$ | radial coordinate of $i^{th}$ point in nozzle inner wall | $x_{NC,i}$ | axial coordinate of $i^{th}$ point in mid-surface profile |
| $R_{9O}$ | *outer radius at core nozzle exit* | $x_{NI,i}$ | axial coordinate of $i^{th}$ point in nozzle inner wall |
| $R_{EC}$ | *radius at mid-surface profile exit* | | |
| $R_{NO, i}$ | radial coordinate of $i^{th}$ point in nozzle outer wall | $x_{NO,i}$ | axial coordinate of $i^{th}$ point in nozzle outer wall |
| | | $\gamma_{NC,i}$ | arctangent of the mid-surface profile slope at $i^{th}$ point |

## 1. INTRODUCTION

High Bypass Raito (HBPR) turbofan has become the most popular power plant for civil airliners. To reduce fuel consumption, pollution emission and noise further, the turbofan engine for civil airliners is developing towards ultra-high bypass ratio (UHBPR) geared turbofan with higher bypass ratio (Birch *et al.* 2000) and lower fan pressure ratio (Cumpsty 2010) to achieve the goals of environmental protection proposed by Advisory Council for Aeronautics Research in Europe (ACARE) (European Commission 2011; Advisory Council for Aviation Research 2012) and National Aeronautics and Space Administration (NASA) (Suder 2013). The fan pressure ratio of future turbofans will be below 1.5 (Hughes 2011) and the bypass ratio of future turbofans will be above 15 (Tejero *et al.* 2019). As the main component of the UHBPR turbofan, the exhaust system not only affects the thrust and specific fuel consumption of the engine (Goulos *et al.* 2018; Otter *et al.* 2019) but also influences the jet noise level. The jet noise of the exhaust system is caused by the strong turbulent fluctuation which is produced by the shear flow between high-velocity jet flow and the low-velocity free stream (Aeroengine Design Manual editorial committee 2002). Related Studies show that the jet noise power of the exhaust system is proportional to the eighth power of the jet flow velocity (Aeroengine Design Manual editorial committee 2002). Therefore, considering the jet flow characteristics should correspond to the noise performance of the exhaust system, it is of great significance to research jet flow characteristics of the turbofan exhaust system.

Many researchers have studied the jet flow characteristics of separate exhaust system. Smith *et al.* (1997) simulate the jet characteristics of the axisymmetrical separate exhaust system of turbofan by program NPARC for solving NS equation in the whole flow field and program PAB3D for solving NS equation in the boundary layer and solving full-potential equation in the main flow region. The reliability of the numerical simulation program to simulate the jet flow characteristics of the separate exhaust system is verified. Hsiao *et al.* (1997) investigate the aerodynamic performance and jet characteristics of the HBPR turbofan exhaust system numerically. The effect of the strut, engine mount fairing, bifurcation, aft mount fairing and freestream Mach number on the performance and jet characteristics of turbofan exhaust system were studied. Compared with the axisymmetric nozzles, the nozzle performance decreases and the thrust angle points upward because of the strut, bifurcation and engine mount fairing. The engine mount fairing decreases the velocity coefficient and shortens jet plumes of the nozzle in the leeward direction. Free stream Mach number (0.10-0.25) has a little effect on the nozzle velocity coefficient and thrust angle but affects the nozzle jet spreading obviously. Hunter *et al.* (2005) research the jet-pylon interaction effect by numerical simulation method. Results suggest that the Coanda-effect caused by the curved shelf of pylon directs core flow upward and starts the jet mixing process early. Therefore, the upstream noise of jet plumes increases and the downstream noise of jet plumes decreases. DeBonis (2009) studied the effect of internal wedge deflector for noise reduction on the performance and flow characteristics of the turbofan exhaust system. Results show that the wedge deflector diverts the fan flow to the underside of jet flow and reduces the turbulence energy on this side. Therefore, the noise on the underside of jet flow reduces. However, the turbulence energy on the upside of jet flow increases because the core flow is exposed to the free stream. This causes an unintended noise source. Bridges and Wernet (2002) simulated the jet flow characteristics of the base nozzle, alternating chevron nozzle and flipper tab nozzle. Results show that the enhanced mixing devices increase turbulence energy in the fan/core shear layer while reducing it in the jet mixing region. The mixing enhanced devices have no influence on the integral length scales in the exhaust plumes but affect integral length scales in peak turbulence regions

significantly. Michael *et al.* (2007) measured the jet plumes of the HBPR turbofan exhaust system with BPR equal to 5 using Particle Image Velocimetry (PIV). The influence of pylon and core chevron nozzle on the flow characteristics and noise performance was studied. Results show that the turbulence in the upper part of the jet plumes increases and the lower shear layer turbulence energy reduces. Relative to the baseline nozzle, the core chevron nozzle increases turbulence energy near the nozzle and reduces it further downstream significantly. Thomas *et al.* (2001) studied the effect of chevron and pylon on the jet plumes of turbofan separate exhaust system. Results show that the cross sectional flow contours are lobed patterns. The wake of the pylon distorts these lobed patterns. The relative orientation between the chevron and the pylon has a significant effect on the development of the lobes downstream of the pylon. Thomas and Kinzie (2004) investigate the jet noise of turbofan with BPR equal to 5 and BPR equal to 8 under approach condition and take-off condition. Kang and Wang (2011) studied the effects of core chevron nozzle on the jet flow characteristics and noise performance of separate exhaust systems. Results show that the fan/core shear layer growth because of the streamwise vortexes caused by chevron in comparison to baseline nozzle. The mixture between fan flow and core flow strengthens and the length of high-temperature jet flow reduces obviously. The peak value of velocity and temperature around the centerline decrease. Zhou *et al.* (2020) investigate the shear flow and distribution of vortex sound source for dual flow nozzle using LES. Results show that there is much convection velocity difference between the inner flow and outer flow. The influence of outer flow on the inner flow reduces downstream and the vortex migration is hindered. The vortex sound source concentrates on the internal shear layer. The dominant components were at low frequencies.

In conclusion, the researches on the jet flow of separate exhaust systems mainly focus on the generation and development of vortex in shear layers, the effect of chevron and pylon on the jet flow characteristics and noise performance of the exhaust system. And the researches above mainly focus on the separate exhaust systems with BPR=5~8. Almost all investigations are carried out under the condition with zero angle of attack. However, there is a high angle of attack for the exhaust system under take-off condition near the ground, under which the effect of jet noise is much more significant. Furthermore, with the increase of engine bypass ratio, the thickness of the fan flow wrapped in the high-velocity core flow increases continuously, which will change the jet characteristics of the exhaust system under take-off condition with high angle of attack obviously. So far, there is little public literature on the jet flow characteristics of HBPR or UHBPR turbofan exhaust systems under take-off condition with high angle of attack.

In this paper, a parametric design method for the aerodynamic profile of turbofan separate exhaust system based on initial Class Shape Transformation function (iCST) curves (Zhu and Qin 2014) was developed firstly. HBPR and UHBPR turbofan exhaust systems were designed. Secondly, the jet flow characteristics of the HBPR turbofan separate exhaust system under take-off condition with zero angle of attack were investigated numerically. Then, the jet flow field of HBPR and UHBPR turbofan exhaust systems under take-off condition with high angle of attack was simulated. Finally, the effects of angle of attack and bypass ratio on the jet flow characteristics of the turbofan exhaust system were investigated and the related flow mechanisms were analyzed.

## 2. PARAMETRIC DESIGN METHOD OF SEPARATE EXHAUST SYSTEM

### 2.1 Geometric Model and Parameterized Definition of Exhaust System

Figure1 shows the geometric model used in this paper. The simplified geometric model includes spinner, intake, cowl, and exhaust system. The spinner, intake, and cowl are included to consider the suction effect of the turbofan engine. The exhaust system consists of fan nozzle, core nozzle, core cowl and plug. The effects of the wing, pylon and bifurcation are not considered. Since the parametric design method of intake and cowl can be referred to the literature (Wang *et al.* 2021), the parametric design method of the exhaust system is given in this section only. The exhaust system is axisymmetric without pylon and bifurcation. So the aerodynamic profile design can be simplified to the design of longitudinal profile in any meridian plane. Figure 2 shows the longitudinal profile and the key geometric parameters of the exhaust system referring to the literature (Wang *et al.* 2020). Among the key geometric parameters, $R_{22O}$ and $R_{22I}$



Spinner  Intake  Cowl  Fan Nozzle
Core Cowl  Core Nozzle  Plug
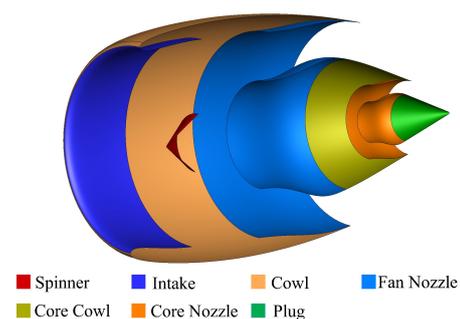
**Fig. 1. Geometric model.**
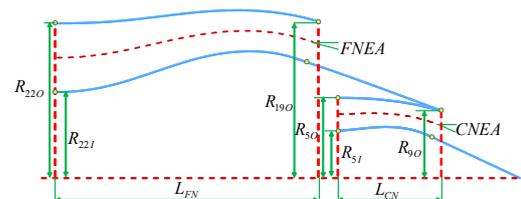


**Fig. 2. Longitude line and key geometric parameters of exhaust system.**

are determined by the inner and outer radius of the fan exit plane. $R_{5O}$ and $R_{5I}$ are determined by the inner and outer radius at the low-pressure turbine exit plane. The other design parameters are determined by the designer.

## 2.2 Nozzle Design

The nozzle is modeled by a mid-surface profile and the area distribution (Wang *et al.* 2014). Nozzle design includes three parts namely calculation of nozzle exit area, mid-surface profile and area distribution design and inner and outer wall design of the nozzle.

### 2.2.1. Calculation of Nozzle Exit Area

The nozzle exit area directly affects the nozzle mass flow rate. And the mass flow rate of the fan nozzle and core nozzle determines the bypass ratio of the turbofan engine, which affects the cooperation and matching of the engine components. The exit area of the fan nozzle and core nozzle can be calculated by the formula (1) and the formula (2) (Liang and Zhao 1998).

$$A_{19} = \frac{W_{13}\sqrt{T_{t13}}}{K\sigma_{FN}p_{t13}q(Ma_{19})} \quad (1)$$

$$A_9 = \frac{W_5\sqrt{T_{t5}}}{K\sigma_{CN}p_{t5}q(Ma_9)} \quad (2)$$

Where $K$ is calculated as

$$K = \sqrt{\frac{k}{R}\left(\frac{2}{k+1}\right)^{-\frac{k+1}{(k-1)}}} \quad (3)$$

$q(Ma)$ is defined as

$$q(Ma) = Ma\left(\frac{2}{k-1}\left(1+\frac{k-1}{2}Ma^2\right)\right)^{-\frac{k+1}{2(k-1)}} \quad (4)$$

The Mach number is calculated by

$$Ma = \begin{cases} \sqrt{\frac{2}{k-1}\left(\left(\frac{p_t}{p_{amb}}\right)^{\frac{k-1}{k}}-1\right)} & \frac{p_t}{p_{amb}} < \left(\frac{p_t}{p_{amb}}\right)_{cr} \\ 1.0 & \frac{p_t}{p_{amb}} \geq \left(\frac{p_t}{p_{amb}}\right)_{cr} \end{cases} \quad (5)$$

Where $(p_t/p_{amb})_{cr}=1.89293$. The fan nozzle exit area should be enlarged properly considering the blockage of the pylon. The available pressure ratio of the core nozzle is lower than the critical pressure ratio usually. The static pressure at the core nozzle exit plane is higher than the ambient pressure due to the effect of the fan flow and the plug. Therefore, the static pressure at the core nozzle exit plane needs to be estimated according to ambient pressure and experience, and then it can be revised according to the preliminary results of the CFD numerical simulation.

### 2.2.2. Mid-surface Profile and Area Distribution

The mid-surface profile determines the shape and bending degree of the nozzle flow passage, which will directly affect the flow acceleration and
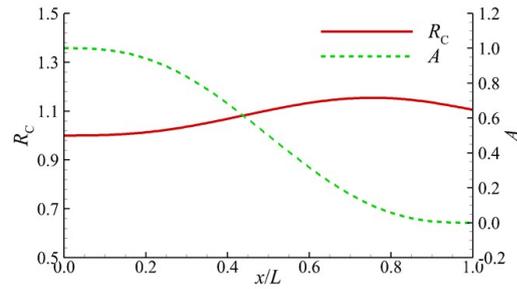


**Fig. 3. Mid-surface profile and area distribution along flow direction.**

deceleration in the nozzle, and then affect the flow loss in the nozzle. The distribution of the flow area of the nozzle will directly affect the distribution of the flow parameters, such as Ma and static pressure, in the nozzle and then affect the aerodynamic performance of the nozzle. The design method of mid-surface profile and area distribution is developed based on iCST curves in this paper. The mid-surface profile of the nozzle is designed with a 4-order pointed nose and pointed aft-end iCST curve. There are five variables to be solved. The constraints are the location $(0, R_{22,O}/2+R_{22,I}/2)$ and slope$(0,0)$ at the starting point and the location $(L_{NC},R_{EC})$, slope$(L_{NC},-\tan(NEA))$ and curvature $(L_{NC},0)$ at the endpoint. The variables can be obtained by solving the linear equations based on the above constraints. Where $L_{NC}$ and $R_{EC}$ can be calculated according to Eqs. (6) and (7).

$$L_{NC} = L_N - \left(R_{EO} - \sqrt{R_{EO}^2 - \frac{A_E}{\pi}}\right)\sin(NEA)/2 \quad (6)$$

$$R_{EC} = R_{EO} - \left(R_{EO} - \sqrt{R_{EO}^2 - \frac{A_E}{\pi}}\right)\cos(NEA)/2 \quad (7)$$

The area distribution is designed by 3-order pointed nose and pointed aft-end iCST curves. There are four variables to be solved. The constraints are the area $(0, \pi(R_{22,O}^2-R_{22,I}^2))$ and rate of area change $(0, 0)$ at starting point and the area $(L_{NC}, A_E)$ and rate of area change $(L_{NC},0)$ at the ending point. Figure 3 shows the mid-surface profile and area distribution of the nozzle as an example.

### 2.2.3. Inner and Outer Wall Design of Nozzle

It can be seen in Fig.4 that the inner and outer wall is the envelope of circles of which the center is on the mid-surface profile and the diameter is the width of the flow passage. For any point $(x_{NC,i}, R_{NC,i})$ $(1<i<I)$ on the mid-surface profile, the width of the flow passage can be calculated as

$$d_i = \frac{A_i}{2\pi R_{NC,i}} \quad (8)$$

The related coordinates of the nozzle inner wall and outer wall are calculated by Eq. (9) (Zhang *et al.* 2014).
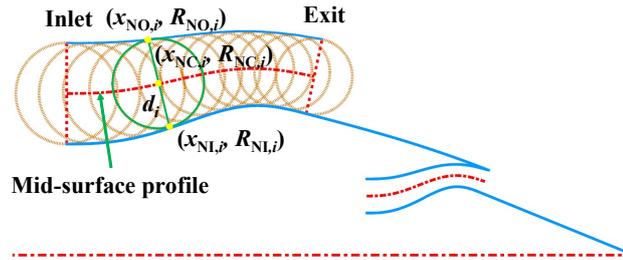
**Fig. 4. Inner wall and outer wall design of nozzle.**

$$x_{NI,i} = x_{NC,i} + \frac{d_i}{2}\sin\left(\gamma_{NC,i}\right)$$

$$R_{NI,i} = R_{NC,i} - \frac{d_i}{2}\cos\left(\gamma_{NC,i}\right)$$

$$x_{NO,i} = x_i - \frac{d_i}{2}\sin\left(\gamma_{NC,i}\right) \qquad (9)$$

$$R_{NO,i} = R_{NC,i} + \frac{d_i}{2}\cos\left(\gamma_{NC,i}\right)$$

## 2.3 Design of Core Cowl and Plug

When the design of the fan nozzle and core nozzle are completed, the core cowl and plug can be designed according to the coordinates, slope and curvature at exit points of the fan nozzle and the core nozzle. The core cowl is designed based on a 4-order iCST curve. There are five variables to be solved. The constraints are the coordinates, slope and curvature at the starting point and the coordinates and slope at the endpoint. The variables can be obtained by solving the linear equations based on the above constraints. The coordinates, slope and curvature at the starting point of the core cowl are equal to the coordinates, slope and curvature at the exit point of the fan nozzle inner wall and the coordinates and slope of the end point of the core cowl are equal to the coordinates and slope at the exit point of the core nozzle outer wall. The plug is designed by line. The coordinates and slope of the starting point are equal to the coordinates and slope at the exit point of the core nozzle inner wall. The radius of the endpoint of the plug is zero. The aerodynamic profile of the exhaust system can be obtained by rotating the longitudinal profile 360° around the engine axis.

The development of exhaust system design method (Wang *et al.* 2014; Zhang *et al.* 2014) based on iCST curves completes the design process, reduces the number of the design variables and makes all the design parameters and geometric constraints intuitiveness for geometrical and physical understanding. The design program of the exhaust system NESDP is developed. Figure 5 presents the aerodynamic profile of the HBPR exhaust system which is designed by the method above.

## 3. NUMERICAL SIMULATION METHOD

To mitigate the computational overhead, half of the model is used for numerical simulation. The
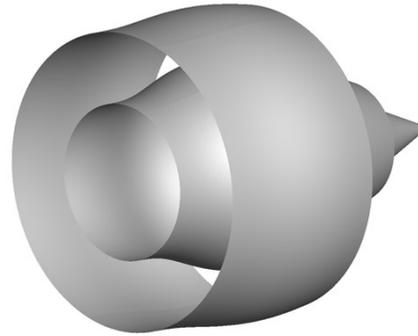


**Fig. 5. Profile of HBPR turbofan exhaust system**

computational domain and boundary condition are shown in Fig. 6. The computational domain is a semi-cylindrical region. The length of the computational domain is 160 times the maximum diameter of the model and the radius of the computational domain is 80 times the maximum diameter of the model referring to the literature (Heidebrecht *et al.* 2016). The multi-block structured grids for the whole computing domain were generated using ICME. All cells adjacent to the wall are refined to ensure that the maximum Y plus of the first cells adjacent to the wall is around one due to the requirements of the turbulence model.

The inlet A and side B of the computational domain are modeled as pressure far-field boundary condition, for which the static pressure, static temperature, Mach number and flow direction are given. The outlet C of the computational domain is applied with the pressure outlet condition, for which a uniformly distributed static pressure is specified. The symmetry plane D is model as a symmetry condition. At the location of the outlet of intake E, the pressure outlet condition is prescribed with specified a targeted mass flow rate. The inlets of the fan nozzle and the core nozzle (F and G) are applied with pressure inlet conditions with uniform distribution of total pressure and total temperature. An impermeable, no-slipped and adiabatic wall boundary condition is applied to the wall of the intake, cowl and exhaust system. The boundary conditions of the intake outlet and the nozzle inlet were acquired by engine performance analysis under take-off condition. The parameters of flight and boundary conditions for HBPR and UHBPR turbofan nacelle under take-off condition are listed in table 1. The angle of attack is 17° under take-off condition with high angle of attack refer to the literature (Andreas *et al.* 2014).
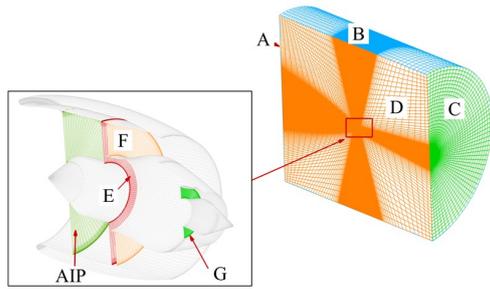
**Fig. 6. Computational domain, mesh generation and boundary conditions.**

**Table 1 Flight and boundary conditions for HBPR and UHBPR turbofan nacelle under take-off condition**

|  | UHBPR | HBPR |
|---|---|---|
| *Ma* | 0.25 | 0.25 |
| *MFCR* | 1.485 | 1.524 |
| *H*, m | 0 | 0 |
| *FNPR* | 1.41 | 1.52 |
| $T_{t13}$,K | 320.1 | 327.0 |
| *CNPR* | 1.29 | 1.32 |
| $T_{t5}$,K | 785.1 | 815.0 |

The commercial flow solver FLUENT is used for all numerical simulations. The three-dimensional steady Reynolds-averaged N-S equations in the conservative form are solved numerically referred by literature (DeBonis 2009). The convection terms are discretized by the second-order upwind scheme and the viscous terms of the equations are discretized by the second-order center scheme. The SST *k-ω* turbulence model was selected referring to the literature (Goulos *et al.* 2016). The implicit density-based algorithm is used to solve the equations. The air is modeled as a compressible ideal gas. The effect of temperature on the thermally physical parameters of the air is modeled by the polynomial method. The molecular viscosity coefficient was calculated by Sutherland's formula.

## 4. RESULTS AND DISCUSSIONS

### 4.1 Validation of Numerical Simulation Method and Grid Independence

To validate the accuracy of the numerical simulation method, the jet characteristics of a single-flow nozzle under subcritical condition were simulated by numerical simulation and the CFD results are compared to the experiment data, which was measured in the Martel facility at the Research Centre for Aerodynamics and Aerothermodynamics in Poitiers, France. The geometric model and experiment data are from the literature (Andersson, *et al.* 2005). The nozzle exit diameter is 50 mm and the Mach number at the nozzle exit plane is 0.75. The pressure ratio of the nozzle is 1.452 and the total temperature at the inlet of the nozzle is 320.4 K, the ambient pressure is 101300 Pa, the static temperature is 288.15 K. The comparison for CFD results and experiment data is presented in Fig. 7.

The circles in red represent experiment data. The solid line in green represents CFD results. Figure 7(a) shows the distribution of axial velocity on the center line in the axial direction. The potential core length define as the axial location where the center line axial velocity is $0.95U_j$. The potential core length is $7.9D_j$ for CFD results and $6.7D_j$ for experiment data. The relative error between the center line axial velocity acquired by CFD and experiment is less than 10%. The reason for this is that only nozzle profile and boundary conditions for CFD is the same as that in experiment but the influence of wind tunnel and measuring equipment on the results is not considered in numerical simulation because of the lack of related information. Although the relative error is large, it is acceptable considering the jet flow characteristics is fairly difficult to simulate accurately. The distribution of axial velocity in the radial direction at the position of $D_j$, $2.5D_j$ and $5D_j$ from nozzle exit are shown in Fig. 7(b). It can be seen that the CFD predictions are in very good agreement with experimental data. The relative error is below 2%. Therefore, it can be concluded that the numerical simulation method above can predict the jet characteristics of the nozzle.
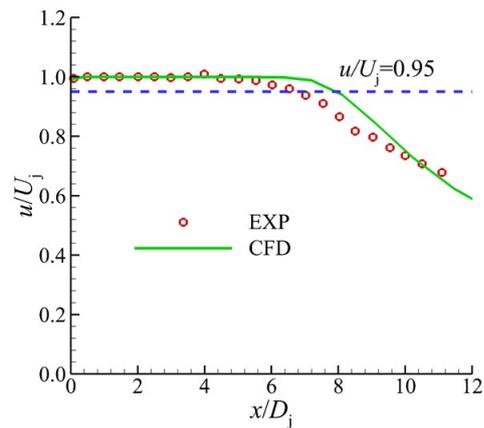


(a) Axial velocity distribution in centerline along axial direction
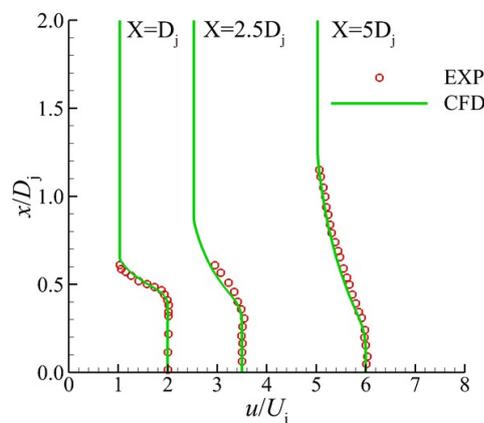


(b) Axial velocity distribution in radial direction at different axial location

**Fig. 7. Comparison for CFD results and experiments data.**

The mesh size (cells number) causes uncertainty of the numerical results, too. Three grids, Grid1 with 2.12 million cells, Grid2 with 4.6 million cells and Grid3 with 9.72 million cells are used in numerical simulation to evaluate the effect of mesh size on the jet characteristics of the UHBPR turbofan exhaust system. The distribution of Mach number for different Grids in the axial direction is presented in Fig. 8 (a). And the distribution of Mach number at the location of $1.9D_{19}$, and $14.9D_{19}$ from nozzle exit for different Grids in the radial direction are presented in Fig. 8 (b). It can be seen from Fig. 8 (a) that the maximum local error of Mach number on center line is less than one percent. And the maximum local error of Mach number between Grid2 and Grid3 is less than that between Grid1 and Grid2. It can be seen from Fig. 8 (b) that the Mach number distribution in the radial direction at the location of $1.9D_{19}$ from the end of the plug for different grids is coincident. For the Mach number distribution in the radial direction at the location of $14.9D_{19}$ from the end of the plug, the maximum local relative error of Mach number between the Grid1 and Grid2 is 1.5% and the maximum local relative error of Mach number between the Grid2 and Grid3 is 0.7%. The reference values are the local Mach number simulated by Grid2. It can be concluded that uncertainty of mesh size can be neglected for Grid 2 which is used for numerical simulation in this paper.
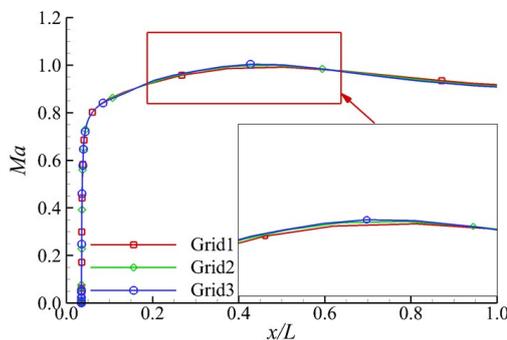


(a) Mach number distribution in centerline along axial direction
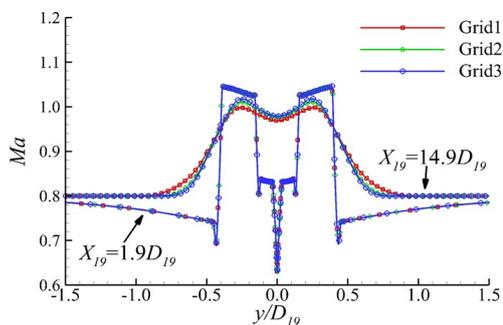


(b) Mach number distribution in radial direction at axial location of $1.9D_{19}$ and $14.9D_{19}$ from the end of plug

**Fig. 8. Grid independence.**

## 4.2 Jet Characteristics of Exhaust System under Take-off Condition with Zero Angle of Attack

The isoline of jet velocity in symmetry plane under take-off condition with zero angle of attack is shown in Fig. 9. The flow field of jet velocity is divided into six regions by the outer boundary (EB1) and the inner boundary (IB1) of the free stream/fan shear layer, the outer boundary (EB2) and the inner boundary (IB2) of the fan/core shear layer and the outer boundary of plug wake (EB3). There are plug wake 1, core flow 2, the fan/core shear layer 3, the fan flow 4, the free stream/fan shear layer 5 and free stream 6. The scale of the free stream/fan shear layer is larger than that of fan/core shear layer since the fan flow velocity relative to free stream is more than that relative to core flow and the velocity gradient in the free stream/fan shear layer is larger than that in fan/core shear layer. Figure 10 presents the cross sectional velocity at five selected axial positions which are $0.54D_{19}$, $1.48D_{19}$, and $2.97D_{19}$, $5.21D_{19}$ and $8.19D_{19}$ from the end of the plug respectively. It can be seen that the center of the round plug wake is the intersection of the engine axis and this cross section. The core flow 2, the fan/core shear layer 3, the fan flow 4, the free stream/fan shear layer 5 and free stream 6 are concentric rings. With plug wake 1 as a center, core flow 2, fan/core shear layer 3, fan flow 4, free steam/fan shear layer 5 and free stream flow 6 are wrapped around the round plug wake 1 from inside out at axial positions of $\Delta x/D_{19}$=0.54, 1.48 and 2.97. And then, the plug wake, the core zone of fan flow and core flow disappear. With core flow as center, the fan flow and free stream are wrapped around the round core flow at the axial positions of $\Delta x/D_{19}$=5.21 and 8.19. The jet flow field of the exhaust system is axisymmetric approximately with the engine axis as an axis.

Figure 11 shows the cross sectional vorticity at the five axial positions. It can be seen that there is an annular high-intensity vorticity region downstream of the fan nozzle exit. It is caused by a large velocity gradient in the free steam/fan shear layer since a fairly large fan flow velocity is relative to the free stream. The vorticity intensity is attenuated on and on, and the radial range of high-intensity vorticity is enlarged toward to downstream in the flow direction. The vorticity distribution downstream of the core nozzle exit plane is similar to that downstream of the fan nozzle exit plane. There is a high-vorticity region downstream of the plug end. It is caused by a large velocity gradient in the plug wake and core flow mixing region. Its intensity is attenuated constantly along the flow direction and the region of high vorticity decreases and disappears finally. The outer high-vorticity region is larger than the inner high-vorticity region since the fan flow velocity($\approx$280m/s) relative to free stream($\approx$80m/s) is more than that relative to core flow($\approx$350m/s) and the velocity gradient in the free stream/fan shear layer is larger than that in fan/core shear layer.
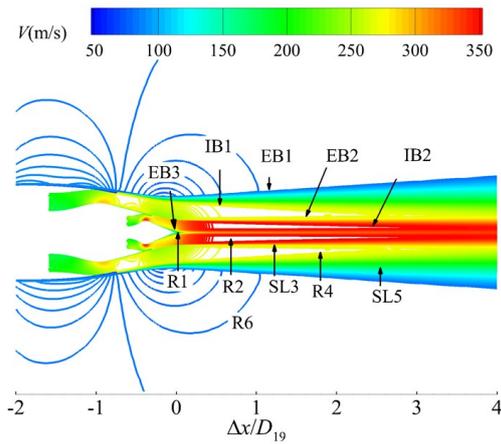
**Fig. 9. Isoline of jet velocity for HBPR turbofan exhaust system in symmetric plane under zero angle of attack.**
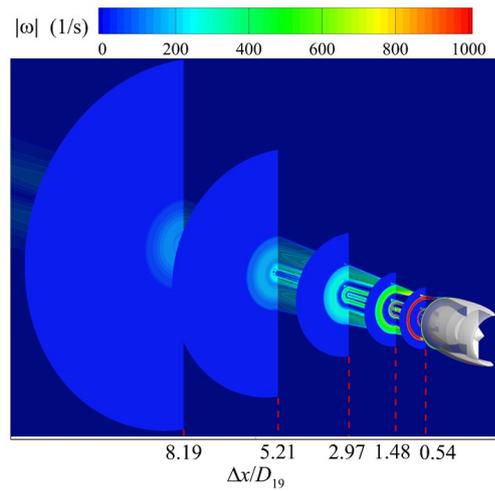


**Fig. 11. Vorticity contour in symmetric plane and cross sectional planes under zero angle of attack.**
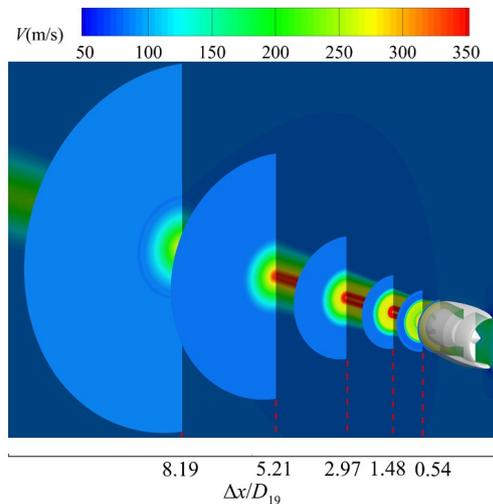


**Fig. 10. Velocity contour in symmetric plane and cross sectional planes under zero angle of attack.**
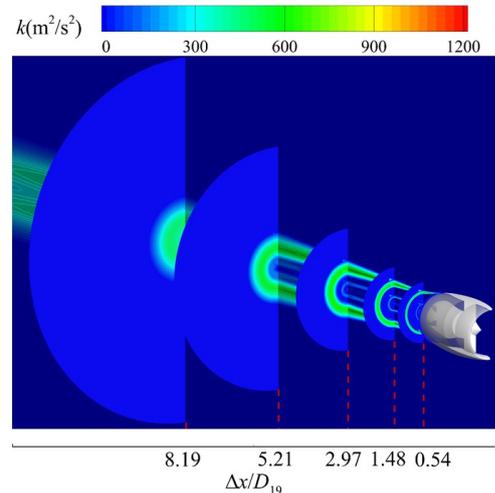


**Fig. 12. Turbulence kinetic energy contour in symmetric plane and cross sectional planes under zero angle of attack.**

Figure 12 shows the cross sectional turbulence kinetic energy at the five axial positions in Fig. 10. It can be seen that there is an annular high turbulence kinetic energy region downstream of the fan nozzle exit plane. The turbulence kinetic energy increases firstly and then decreases along the flow direction. So, there is a peak in turbulence kinetic energy along the flow direction. The turbulence kinetic energy contour downstream of the core nozzle exit plane is similar to that downstream of the fan nozzle exit plane. However, the turbulence kinetic energy level and range of high turbulence kinetic energy region downstream of the core nozzle exit plane are much lower than that of the fan nozzle exit plane.

### 4.3 Effects of Angle of Attack on the Jet Flow Characteristics under Take-off Condition

The comparison for jet velocity, vorticity, and turbulence kinetic energy under take-off condition

with zero and high angle of attack is presented in Fig. 13. It can be seen from Fig. 13(a) that the high angle of attack of free stream direct the exhaust plumes upward under take-off condition. While it is difficult to quantify, the high-velocity region in exhaust plumes under take-off condition with high angle of attack does appear to have shortened. The high-velocity region in which the velocity is larger than three-fourths maximum velocity shortens by 55.1%. It can be seen from Fig. 13(b) that the upward jet flow velocity and shear layers direct the high-vorticity region upward. The high-vorticity region caused by the free stream/fan shear layer and the high vorticity region caused by the fan/core shear layer under take-off condition with zero angle of attack is separate nearly. However, the high-vorticity region generated by free stream, fan flow and core flow mix along the flow direction under take-off condition with high angle of attack. The

(a) Velocity

(b) Vorticty



(c) Turbulence kinetic energy
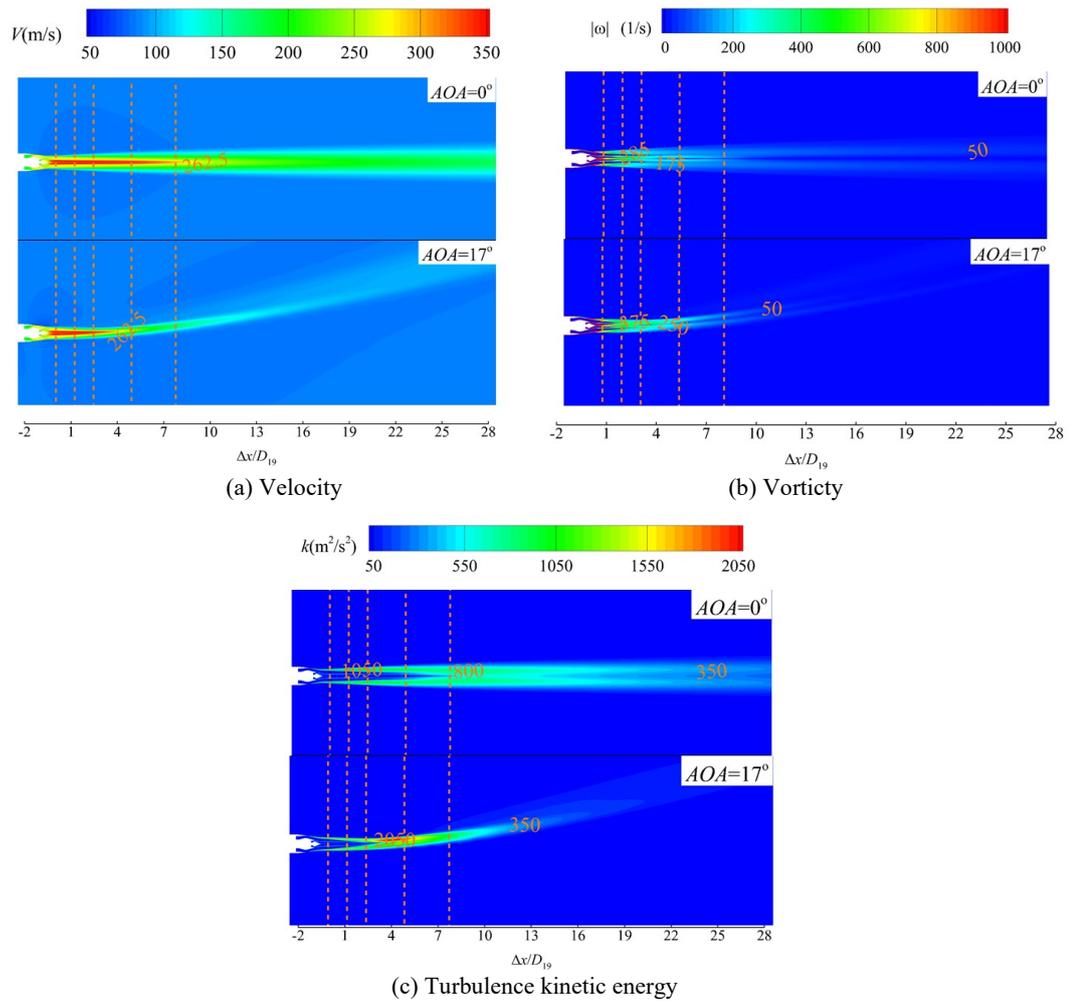
**Fig. 13. Comparison for flow parameters in symmetric plane under take-off condition with zero and high angle of attack.**

high-vorticity region in which the vorticity is higher than 5% maximum values in legend shortens by 47.7%. The vorticity level increases by around 30% within the range of $0.5D_{19}$ to $3.5D_{19}$ from the end of the plug. Figure 13(c) shows that the turbulence kinetic energy comparison for jet flow under take-off condition with zero and high angle of attack. The upward high-velocity region, shear layers and high-vorticity region direct the high turbulence kinetic energy region upward. The high kinetic turbulence energy region in which the turbulence kinetic energy is higher than one-third of maximum turbulence energy in the jet flow of the HBPR turbofan exhaust system shortens by 50.9%. However, the peak value of turbulence kinetic energy on the upper side of the exhaust plumes increases by 87%.

Figure 14 shows the velocity, vorticity and turbulence kinetic energy comparison for jet flow in five cross sections with zero and high angle of attack. The positions of cross sections 1, 2, 3, 4 and 5 are $0.54D_{19}$, $1.48D_{19}$, $2.97D_{19}$, $5.21D_{19}$ and $8.19D_{19}$ from the end of the plug respectively. It can be seen that the contour of the jet velocity of the exhaust system under take-off condition with hig

angle of attack in cross section 1 is the same as that under take-off condition with zero angle of attack. The jet flow velocity at cross section 2, 3, 4 and 5 are concentric circles under take-off condition with zero angle of attack. However, under take-off condition with high angle of attack, the jet flow velocity in cross section 2 is flattened slightly at the top of the high-velocity region. The jet flow velocity in cross section 3 is concave in the middle at the top of the high-velocity region and is raised on both sides at the top of the high-velocity region. In cross section 4, the core flow velocity is higher than the fan flow velocity slightly under take-off condition with high angle of attack, while the core flow velocity is much higher than the fan flow velocity under the take-off condition with zero angle of attack. The concave region in the middle at the top of the high-velocity region and the raised region on both sides at the top of the high-velocity region are more obvious than that in cross section 3. In cross section 5, fan flow and core flow are integrated. The shape of jet flow is like a horseshoe.

The distribution of the high-vorticity region is affected by the shape of the free stream/fan flow shear layer and fan/core flow shear layer. Figure
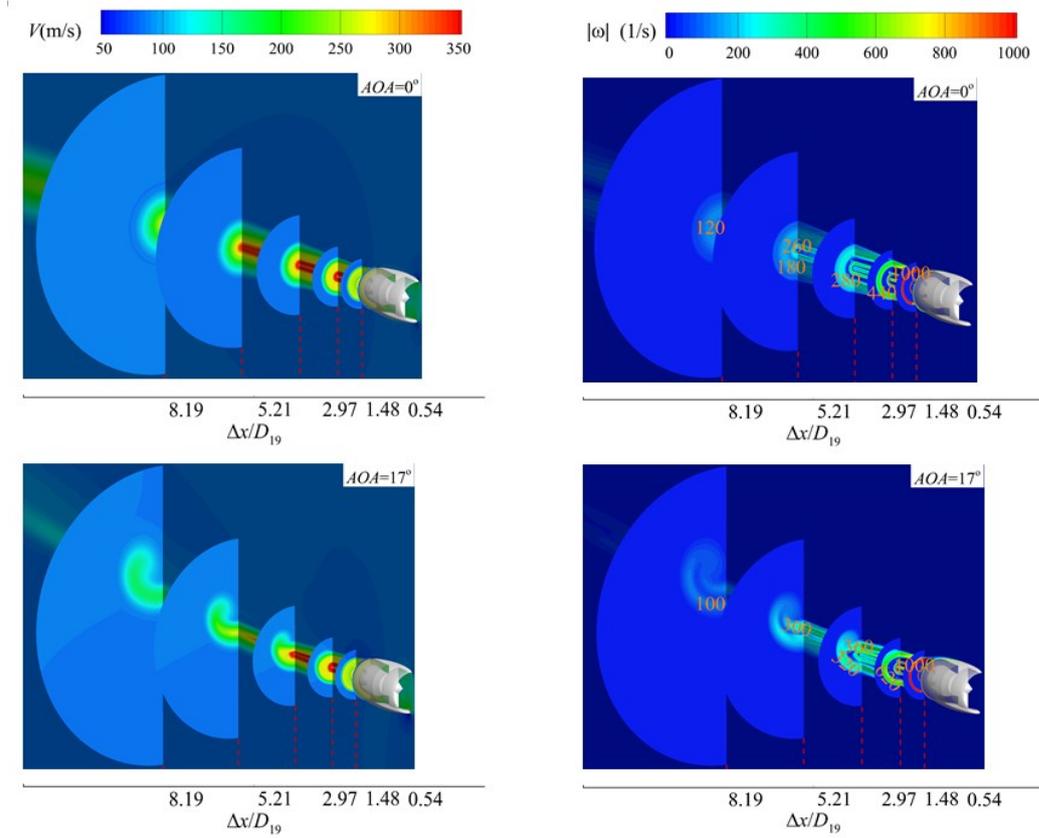
(a) Velocity



(b) Vorticity
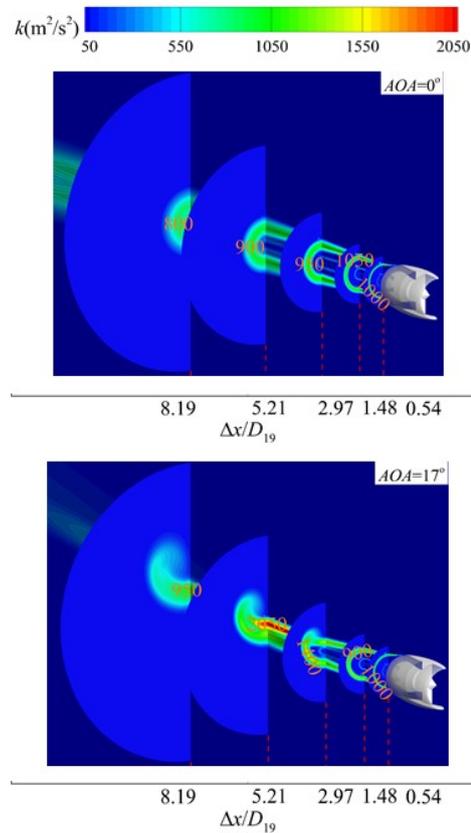


(c) Turbulence kinetic energy

**Fig. 14. Comparison for jet flow parameters of HBPR turbofan exhaust system under take-off condition with zero and high angle of attack.**

14(b) shows the vorticity of jet flow at the five cross sections under take-off condition with zero angle of attack and high angle of attack. It can be seen that the vorticity of jet flow in the cross section under take-off condition with zero angle of attack is axisymmetric. However, under take-off condition with high angle of attack, the vorticity of jet flow in cross section 1 is flattened slightly at the top of the annular high-vorticity region, which is caused by the free stream/fan flow shear layer. The vorticity of jet flow in cross section 2 is similar to that in cross section 1 and is raised on both sides at the top of the high-velocity region obviously. The vorticity of jet flow in cross section 3 is concave in the middle and raised on both sides at the top of the high-vorticity region. The high-vorticity region caused by the free stream/fan flow shear layer and the high-vorticity region caused by the fan/core shear layer mix with each other together. The outline of the high-vorticity region caused by the free stream/fan flow shear layer is like a horseshoe. The jet flow of the fan nozzle and core nozzle mix completely in cross section 4. The vorticity intensity in the middle at the top of the high -vorticity region under take-off condition with high angle of attack is larger than that under take-off condition with zero angle of attack. The vorticity intensity in cross section 5 is lower than that in cross section 4 obviously.

The change of velocity and vorticity distribution of jet flow changes the distribution of turbulence kinetic energy. Figure 14(c) shows the cross sectional turbulence kinetic energy at five axial positions. It can be seen that the turbulence kinetic energy in cross section 1 under take-off condition with zero angle of attack are two concentric rings and it is almost the same as that in cross section 1 under take-off condition with high angle of attack. The turbulence kinetic energy is flattened slightly in the middle at the top of the high turbulence kinetic energy region under take-off condition with high angle of attack while the contour of the jet flow is concentric rings with zero angle of attack in cross section 2. And the turbulence kinetic energy level of the high turbulence energy region is higher under take-off condition with high angle of attack. In cross section 3, the high turbulence kinetic energy region generated by the free stream/fan shear layer and the fan/core shear layer are integrated, while that is almost separate under take-off condition with zero angle of attack. The peak value of turbulence kinetic energy in jet flow under take-off condition with high angle of attack increases by 47.3%. The high turbulence kinetic energy region in cross section 4 is smaller than that in cross section 3 under take-off condition with high angle of attack while the turbulence kinetic energy intensity in the middle at the top of high turbulence kinetic energy region increases. And the peak value of turbulence kinetic energy is 127.8% higher than that under take-off condition with zero angle of attack in cross section 4. The large velocity gradient in this region causes severe shear and high-intensity vortex due to the high-velocity core flow is exposed to the low-velocity free stream under take-off condition with high angle of attack. In cross section 5, the distribution of turbulence kinetic energy is more uniform under take-off condition with high angle of attack. The outline of the high turbulence kinetic energy region is like a horseshoe, similar to the distribution of the high-velocity region and high-vorticity region.

To analyze the influence mechanism of the angle of attack on the jet characteristics of the exhaust system, the streamline of jet flow under take-off condition with zero and high angle of attack is presented in Fig. 15. The streamline of the free stream is marked in red. The streamline of fan flow is marked in rainbow and the streamline in core flow is marked in blue. It can be seen from Fig. 15(a) that the fan flow is wrapped around the core flow which is axisymmetric with the engine axis as the axis. And the free stream is wrapped around the fan flow. So, the mixture of free stream, fan flow and core flow caused by the velocity gradient appears in the shear layers only. It can be seen from Fig. 15(b) that the flow angle of the free stream relative to the jet flow of the exhaust system directs the exhaust plumes upward. The flow separations appear in the lee area at the back of the cowl and jet flow when free stream flow around the cowl and the jet flow of exhaust system. So, there are a pair of vortexes. Only one can be seen because the half of model is shown in Fig. 15(b). On the one hand, the free stream was involved in fan flow by the vortexes and on the other hand, the fan flow was involved in the free stream, too. The vortexes strengthen and their scope increase constantly along the flow direction. The core flow was involved in the free stream and the free stream was involved in core flow at the axial location of four times $D_{19}$ from the end of the plug. The vortexes decay constantly and disappear finally along the flow direction due to viscous dissipation. The vortexes in the lee area at the back of the cowl and the jet flow lead to secondary flow in the cross sectional plane.



**(a)** *AOA*=0°



**(b)** *AOA*=17°
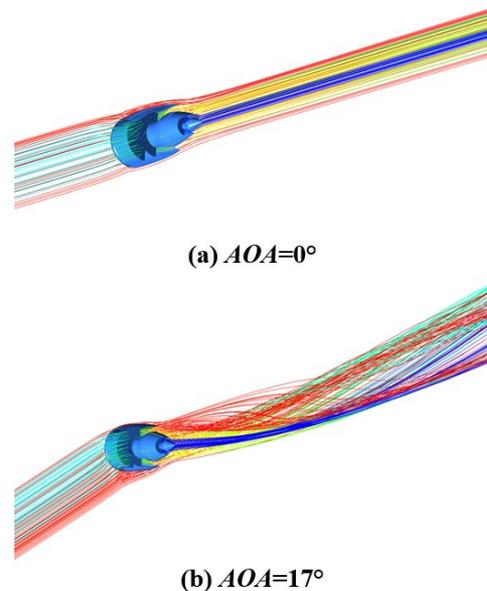
**Fig. 15. Comparison for streamline of nacelle under take-off condition with zero and high angle of attack.**

The secondary flow leads to the macro relative flow among the free stream, fan flow and core flow. The mixture of free stream, fan flow and core flow strengthens. At the same time, the outline of cross sectional high-velocity region from round to U shape and turn into horseshoe finally. The contact area among the free stream, fan flow and core flow increase. The large velocity gradient region appears since the vortexes expose high-velocity core flow to the low-velocity free stream. The mixture of the free stream, the fan flow and the core flow are strengthened by increased contact area and large velocity gradient region. The length of the high-velocity region, high-vorticity region and high turbulence kinetic energy region shorten and the peak value of turbulence kinetic energy increases obviously due to the enhanced mixture among the free stream, the fan flow and the core flow.

In conclusion, the mixture of free stream, fan flow and core flow is enhanced and the vorticity and turbulence kinetic energy increase sharply downstream nozzle exit. Furthermore, the length of exhaust plumes shortens under take-off condition with high angle of attack. The reason for this is that the vortexes in the lee area at the back of the cowl and jet flow leads to cross sectional secondary flow in the jet flow field. The secondary flow causes the macro relative flow and expose high-velocity core flow to low-velocity freestream, which increases the contact area and velocity gradient among the free stream, fan flow and core flow.

## 4.4 Effect of Bypass Ratio on the Jet Flow Characteristics under Take-off Condition

Although the Mach number of core flow is smaller than that of fan flow, the velocity of core flow is much higher because the temperature of core flow is much higher. The large velocity gradient in the shear layer between the free stream and core flow can be alleviated or avoided by thickening the fan flow wrapped around the core flow. So the jet flow characteristics of the exhaust system are affected by the bypass ratio of the turbofan significantly. In this section, the influence of the bypass ratio on the jet flow characteristics of the exhaust system will be studied by comparing jet flow characteristic of the HBPR turbofan exhaust system (BPR=10) with that of UHBPR turbofan exhausts system (BPR=15) under take-off condition with high angle of attack. And the related flow mechanism will be analyzed.

Figure 16 presents the comparison for a profile of HBPR nacelle and UHBPR nacelle in a symmetric plane. The design parameters of the UBHPR and HBPR turbofan exhaust systems are not the same due to the difference in aerodynamic conditions and geometric constraints. The length diameter ratio of fan nozzle reduces in order to ensure that the ratio of the outer diameter of core nozzle exit to the inner diameter of fan nozzle exit and the length diameter ratio of core cowl are the same because they have a greater impact on the performance of exhaust system. The other design parameters of the UHBPR and HBPR turbofan exhaust systems are the same.
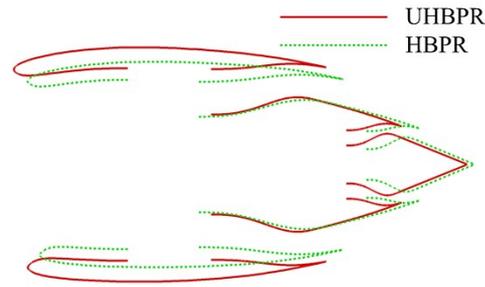


**Fig. 16. Comparison for the profile in symmetric plane of HBPR/ UHBPR turbofan nacelle.**

**Table 2 Key Parameters of HBPR and UHBPR Exhaust Systems**

|  | UHBPR | HBPR |
|---|---|---|
| $L_{FN}/D_{22O}$ | 0.6 | 0.87 |
| $D_{19O}/D_m$ | 1.266 | 1.266 |
| $FNEA,°$ | 12 | 12 |
| $L_{CN}/D_{5O}$ | 0.8 | 0.8 |
| $R_{9O}/R_{19I}$ | 0.6 | 0.6 |
| $CNEA,°$ | 19 | 19 |

The design parameters of the UHBPR and HBPR turbofan exhaust systems are listed in Table 2.

Figure 17, Fig. 18 and Fig. 19 show distribution of jet velocity, vorticity and turbulence kinetic energy of the HBPR and UHBPR turbofan exhaust systems at symmetric plane and four cross sections. The positions of cross sections 1, 2, 3 and 4 are $0.88D_{19}$, $2.53D_{19}$, $5.01D_{19}$ and $8.31D_{19}$ from the end of the plug respectively. The jet velocity in the symmetry plane is shown in Fig. 17(a). It can be seen that the peak value of jet flow velocity of the UHBPR turbofan exhaust system is 5.5% lower than that of the HBPR turbofan exhaust system. But the length of the high-velocity region is almost the same. The cross sectional velocity in jet flow at four positions is shown in Fig. 17(b). It can be seen that the jet flow velocity in cross sections for the UBHPR turbofan exhaust system is similar to that for the HBPR turbofan exhaust system. The high-velocity region of the UHBPR turbofan exhaust system in cross section 1 and 2 is much larger than that of the HBPR turbofan exhaust system due to the mass flow rate of the UHBPR turbofan fan nozzle is much larger. The jet flow velocity of the UBHPR turbofan exhaust system is lower than that of the HBPR turbofan exhaust system slightly due to the lower total pressure and total temperature at the inlet of nozzles. The high-velocity region of the UHBPR turbofan exhaust system is almost the same as that of the HBPR turbofan exhaust system in cross section 3 and 4. The peak value in the high-velocity region is higher slightly for the HBPR turbofan exhaust system in cross section 3 while it is lower in cross section 4. The reason for this is that the fan flow velocity of the UHBPR turbofan exhaust system is lower than that of the HBPR turbofan exhaust system. This leads to a lower velocity gradient in the free stream/fan shear layer
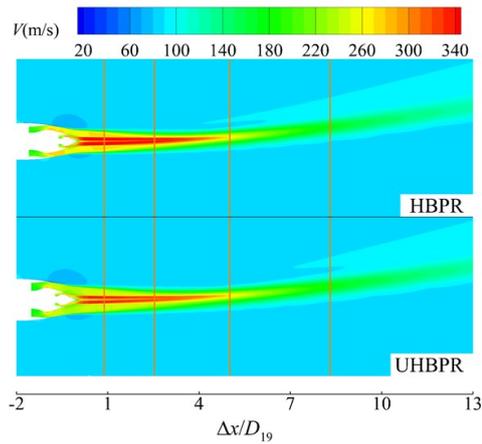
(a) Velocity in symmetric plane
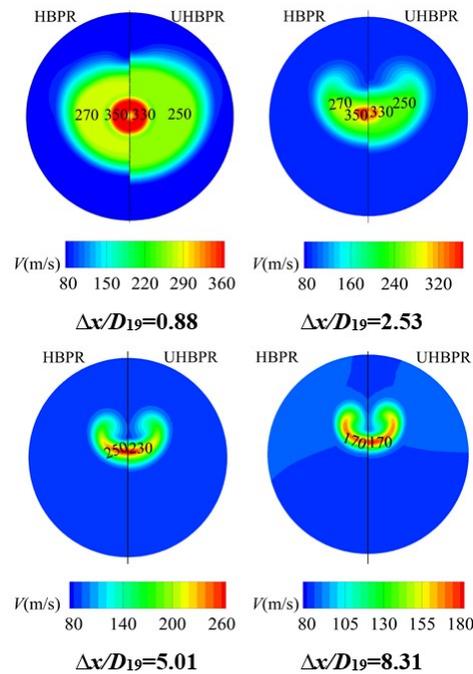


(b) Cross sectional velocity at four selected axial positions

**Fig. 17. Comparison for jet velocity.**
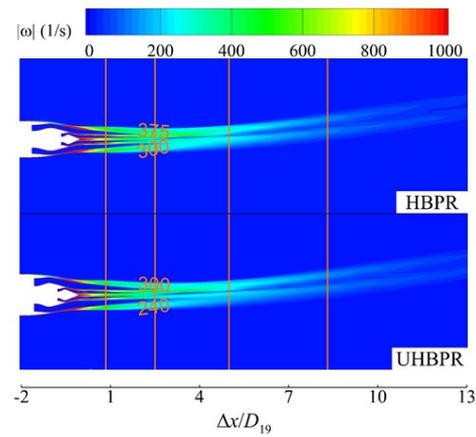


(a) Vorticity in symmetric plane
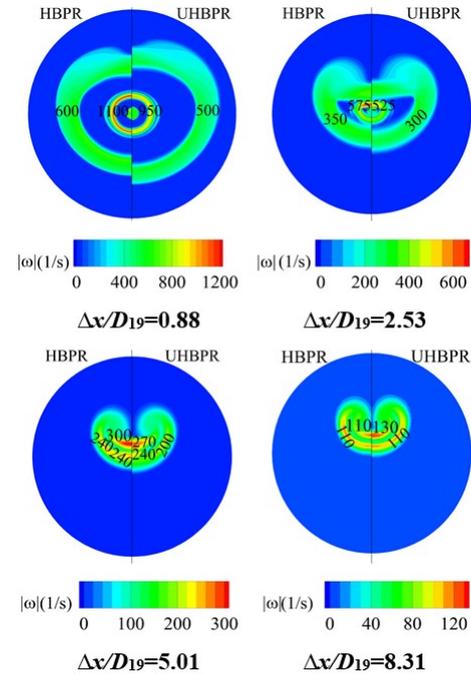


(b) Cross sectional vorticity at four selected axial positions

**Fig. 18. Comparison for vorticity.**

and a slower mixture between the free stream and fan flow.

It can be seen from Fig. 18(a) that the vorticity level in the symmetric plane of the UHBPR turbofan exhaust system is lower than that of the HBPR turbofan exhaust system since the jet flow velocity relative to free stream is lower. It can be seen from Fig. 18(b) that the distribution of cross sectional vorticity at four axial positions for the UHBPR turbofan exhaust system is similar to that for the HBPR turbofan exhaust system. In cross section 1, 2 and 3 the high-vorticity region of the UHBPR turbofan exhaust system is larger than that of the HBPR turbofan exhaust system. The vorticity level of the high-vorticity region is lower for the UHBPR turbofan exhaust system. In cross section 4 the area of the high-vorticity region for the UHBPR turbofan

exhaust system is almost the same as that for the HBPR turbofan exhaust system. However, the vorticity level of the high-vorticity region for the UHBPR turbofan exhaust system is larger slightly.

The contour of turbulence kinetic energy in the symmetric plane is shown in Fig. 19 (a) and the contours of cross sectional turbulence kinetic energy at four axial positions are shown in Fig. 19(b). It can be seen from Fig. 19(a) that the area of high turbulence kinetic energy region in jet flow for UHBPR turbofan exhaust system is almost the same as that for HBPR turbofan exhaust system. However, the high turbulence kinetic energy level peak on the upper side of the UHBPR turbofan exhaust plume is 29.3% lower than that of the HBPR turbofan exhaust plumes. It can be seen in Fig. 19(b) that the peak value of high turbulence
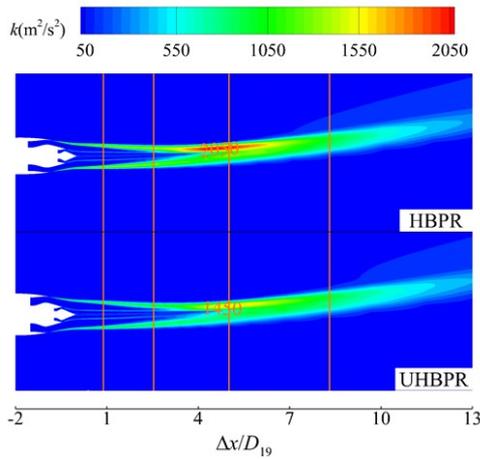
(a) Turbulence kinetic energy in symmetric plane
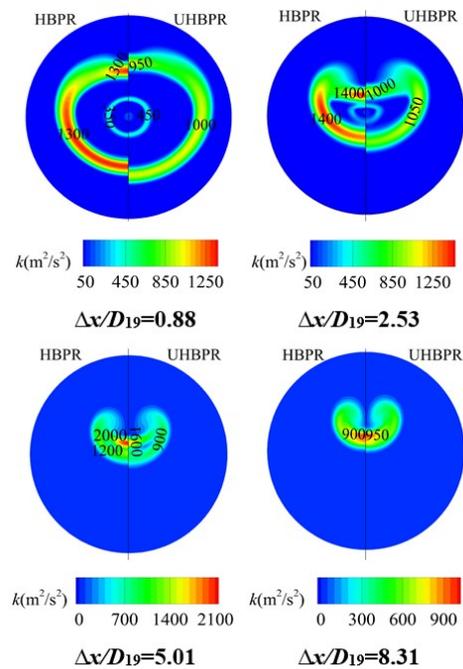


(b) Cross sectional turbulence kinetic energy at four selected axial positions

**Fig. 19. Comparison for turbulence kinetic energy.**

kinetic energy region in jet flow for UHBPR turbofan exhaust system is around 27% smaller than that for HBPR turbofan exhaust system in cross section 1 and 2. There is a region in which the turbulence kinetic energy for the HBPR turbofan exhaust system is higher than the peak value of turbulence kinetic energy for the UHBPR turbofan exhaust system in jet flow. And in cross section 3, the peak value of high turbulence kinetic energy region for UHBPR turbofan exhaust system in jet flow is around 20% lower and the maximum value of turbulence kinetic energy in the free stream/fan shear layer is around 25% lower than that for HBPR turbofan exhaust system. However, the peak value of turbulence kinetic energy in cross section 4 for the UHBPR turbofan exhaust system is 5.6% higher. This means that the turbulence kinetic energy for the UHBPR turbofan exhaust system in

jet flow attenuates more slowly from cross section 3 to 4.

The jet velocity decreases obviously due to lower total pressure and total temperature at the inlet of nozzle seen from Table 1 for the UHBPR turbofan exhaust system. This leads to lower jet flow velocity relative to free stream and slower mixture in free stream/fan shear layer and fan/core shear layer. This is the reason for that the level of high vorticity region and high turbulence kinetic energy region reduces. In the meantime, the fan flow wrapped in high-velocity core flow is thicker for the UHBPR turbofan exhaust system, because of the higher bypass ratio. The peak value of the high-vorticity region and high turbulence kinetic energy region under take-off condition with high angle of attack decreases. The reasons are that the contact area between the high-velocity core flow and the low-velocity free stream decreases due to thicker fan flow and the velocity gradient in the core flow and free stream mixing region decreases because of lower core flow. Meanwhile, the velocity, vorticity and turbulence kinetic energy in jet flow for the UHBPR turbofan exhaust system attenuates more slowly due to the lower and thicker fan flow.

## 5. CONCLUSION

In this paper, a parametric design method for separate exhaust system based on iCST curves was developed. HBPR and UHBPR turbofan separate exhaust systems were designed. Furthermore, the flow characteristics of the HBPR turbofan exhaust system under take-off condition with zero angle of attack and high angle of attack were studied. The flow characteristics of the UHBPR turbofan exhaust system under take-off condition with high angle of attack were simulated. The effects of angle of attack and bypass ratio on the jet flow characteristics were investigated and the related flow mechanisms were analyzed. Our conclusions are as follows:

1.  The axisymmetric exhaust plumes of the HBPR turbofan exhaust system are distributed around the engine axis under take-off condition with zero angle of attack. With the plug wake as a center, the core flow, the fan/core shear layer, the fan flow, the free stream/fan shear layer and the free stream flow were wrapped around the plug wake from inside out. The dual annular high-vorticity region caused by the free stream/fan shear layer and fan/core shear layer is attenuated on and on along flow direction. The turbulence kinetic energy increases firstly and then decreases. There is a turbulence kinetic energy level peak along the flow direction.

2.  The flow angle of the free stream relative to the jet flow of the exhaust system directs the exhaust plumes upward. There are vortexes in the lee area at the back of the cowl and the jet flow under take-off condition with high angle of attack. The vortexes lead to complex secondary flow in cross section and expose the high-velocity core flow to the low-velocity free

stream. The contact area and velocity gradient in mixing region among the free stream, fan flow and core flow were increased. Therefore, the mixture of jet flow and free stream strengthens. Compared with the jet flow of HBPR turbofan exhaust system under take-off condition with zero angle of attack, the length of the high-velocity region, high-vorticity region and high turbulence kinetic energy region shorten by 55.1%, 47.7% and 50.9% respectively and the level of high-vorticity region and the turbulence kinetic energy peak on the upper side of exhaust plumes increase by around 30% and 87% respectively.

3. Under take-off condition with high angle of attack, the jet velocity of the UHBPR turbofan exhaust system decreases by 5.5% due to the lower total pressure and total temperature at the inlet of the nozzle. The vorticity and turbulence kinetic energy decrease due to decreased fan flow velocity relative to the free stream. And the peak value of turbulence kinetic energy on the upper side of the UHBPR turbofan exhaust plumes is 29.3% lower than that of the HBPR turbofan jet plumes. The reasons are that the contact area between high-velocity core flow and the free stream decreases due to the thicker fan flow and the velocity gradient in the core flow and free stream mixing region decreases because of the lower core flow velocity.

The jet flow characteristics of the HBPR and UHBPR turbofan exhaust systems under take-off condition with high angle of attack are studied in this paper with the suction effect of intake considered only. The noise performance and the effects of the wing, pylon and nozzle chevron on the aerodynamic and noise performance under take-off condition with high angle of attack need to be investigated further.

## ACKNOWLEDGEMENTS

## REFERENCES

*Advisory Council for Aviation Research* (2012). Realizing Europe' Vision for Aviation. Strategic Research & Innovation Agenda. European Commission.

*Aeroengine Design Manual editorial committee* (2002). Aeroengine Design Manual Volume 7 Intake and exhaust system design. Beijing:

Aviation Industry Press.

Andersson, N., L. E. Eriksson and L. Davidson (2005). Large-Eddy Simulation of Subsonic Turbulent Jets and Their Radiated Sound. *AIAA Journal* 43(9), 1899-1912.

Andreas, P., S. S. Zoltán, L. K. Wesley and R. Becky (2014). Ultra-short Nacelles for Low Fan Pressure Ratio Propulsors. *In Proceeding of ASME Turbo Expo* ASME GT2014-26369.

Birch, N. T. (2000). 2020 vision: the prospects for large civil aircraft propulsion. *Aeronautical Journal -New Series* 104(1038), 347-352.

Bridges, J. and M. Wernet (2002). Turbulence measurements of separate flow nozzles with mixing enhancement features. *8th AIAA/CEAS Aeroacoustics Conference* AIAA 2002-2484.

Cumpsty, N. (2010). Preparing for the future: reducing gas turbine environmental impact-IGTI scholar lecture. *Journal of Turbomachinery* 132, 041017.

DeBonis, J. R. (2009). RANS Analyses of Turbofan Nozzles with Internal Wedge Deflectors for Noise Reduction. *Journal of Fluids Engineering* 131(4), 041104.

*European Commission* (2011). Flightpath 2050. Europe' s Vision for Aviation. Report of the High Level Group on Aviation Research.

Goulos, I., T. Stankowski and O. J. Etc (2016). Aerodynamic Design of Separate-Jet Exhausts for Future Civil Aero-engines-Part I: Parametric Geometry Definition and Computational Fluid Dynamics Approach. *Journal of Engineering for Gas Turbines and Power* 138, 081201-1.

Goulos, I., T. Stankowski, D. MacManus, P. Woodrow and C. Sheaf (2018). Civil turbofan engine exhaust aerodynamics: Impact of fan exit flow characteristics. *Aerospace Science and Technology* 73, 85-95.

Heidebrecht, A., T. Stankowski and D. MacManus (2016). Parametric geometry and computational process for turbofan nacelles. *In Proceeding of ASME Turbo Expo* ASME GT2016-57784.

Hsiao, E., M. Su and J. Colehour (1997). Navier-Stokes analysis of a high by-pass engine exhaust system and plume. *15th Applied Aerodynamics Conference* AIAA 1997-2282.13

Hughes, C. (2011). The Promise and Challenges of Ultra High Bypass Ratio Engine Technology and Integration. *AIAA Aero Sciences Meeting.*

Hunter, C., R. Thomas, K. Abdol-Hamid and S. Pao (2005). Computational Analysis of the Flow and Acoustic Effects of jet-pylon Interaction. *11th AIAA/CEAS Aeroacoustics Conference* AIAA 2005-3083.15

Kang, G. Q. and Q. Wang (2011). Numerical

simulation on jet flow field of separate flow nozzles with chevron trailing edge. *Journal of Aerospace Power* 26(1), 154-160.

Liang, D. W. and Y. Zhao (1998). Fundamentals of Fluids Mechanics. Beijing: *Aviation Industry Press*.

Michael, J. D., B. S. Henderson and K. W. Kinzie (2007). Turbulence Measurements of Separate-flow Nozzles with Pylon Interaction Using Particle Image Velocimetry. *AIAA Journal* 45(6), 1281-1289.

Otter, J. J., R. Christie, I. Goulos, D. MacManus and N. Grech (2019). Parametric design of non-axisymmetric separate-jet aero-engine exhaust systems. *Aerospace Science and Technology* 93, 105186.

Smith, C., N. Snyder and B. Vittal (1997). Analysis of an axisymmetric two-stream nozzle plume. *Applied Aerodynamics Conference* AIAA 1997-2283.

Suder, L. K. (2013). NASA Environmentally Responsible Aviation Project's Propulsion Technology Phase I Overview and Highlights of Accomplishments. *51st AIAA Aerospace Sciences Meeting including the New Horizons Forum and Aerospace Exposition* AIAA 2013-0414.

Tejero, F., M. Robinson, G. D. MacManus and C. Sheaf (2019). Multi-objective optimization of short nacelles for high bypass ratio engines. *Aerospace Science and Technology* 91, 410-421.

Thomas, H. R., W. K. Kinzie and S. P. Paul (2001). Computational analysis of a pylon-chevron core nozzle interaction. *7th AIAA/CEAS Aeroacoustics Conference* AIAA 2001-2185.

Thomas, R. and K. Kinzie (2004). Jet-pylon interaction of high bypass ratio separate flow nozzle configurations. *10th AIAA/CEAS Aeroacoustics Conference*. AIAA 2004-2827.

Wang, D., M. H. Cong, Z. Y. Zhang, Y. W. Du and Y. Shi (2014). A Design Method of Turbofan Separate Exhaust System. CN103823921A.

Wang, W. J., B. W. Liu, L. Zhou, Z. X. Wang and W. J. Deng (2021). Parametric Design Method for Aerodynamic Profiles of Continuous Curvature Non-Axisymmetric Nacelle. *Journal of Propulsion Technology* 42(7), 1827-1838.

Wang, W. J., L. Zhou, Z. X. Wang and J. W. Shi. (2020). Influence of Geometric Parameters on Overall Performance of High Bypass Ratio Turbofan Nacelle and Exhaust System. *Journal of Applied Fluid Mechanics* 13(6), 1959-1973.

Zhang, J. D., J. Chen, W. Wang, Y. G. Li and J. J. Liu (2014). A Design Method and Performance Research of Separately Exhaust System. *Aeroengine* 40(2), 47-50, 69.

Zhou, E.C., C. Xu and X.H. Lai (2020). Large eddy simulation of Co-Axial Jets and Analysis of Sound Source. *Journal of Engineering Thermophysics* 41(9), 2199-2206.

Zhu, F. and N. Qin (2014). Intuitive Class/Shape Function Parameterization for Airfoils. *AIAA Journal* 52(1), 17-25.